



AFRL-RX-WP-TR-2016-0012

**METALLIC AND CERAMIC MATERIALS RESEARCH
Task Order 0003: Metallic Materials, Processing and Performance
Development for Air Force Applications**

**Sang-Lan Kim, David S. Lee, Triplicane A. Parthasarathy, Satish I. Rao, Oleg N. Senkov,
James M. Scott, and Vikas Sinha**

UES, Inc.

**OCTOBER 2015
Final Report**

Distribution Statement A. Approved for public release; distribution unlimited.

See additional restrictions described on inside pages

STINFO COPY

**AIR FORCE RESEARCH LABORATORY
MATERIALS AND MANUFACTURING DIRECTORATE
WRIGHT-PATTERSON AIR FORCE BASE, OH 45433-7750
AIR FORCE MATERIEL COMMAND
UNITED STATES AIR FORCE**

NOTICE AND SIGNATURE PAGE

Using Government drawings, specifications, or other data included in this document for any purpose other than Government procurement does not in any way obligate the U.S. Government. The fact that the Government formulated or supplied the drawings, specifications, or other data does not license the holder or any other person or corporation; or convey any rights or permission to manufacture, use, or sell any patented invention that may relate to them.

This report was cleared for public release by the USAF 88th Air Base Wing (88 ABW) Public Affairs Office (PAO) and is available to the general public, including foreign nationals.

Copies may be obtained from the Defense Technical Information Center (DTIC) (<http://www.dtic.mil>).

AFRL-RX-WP-TR-2016-0012 HAS BEEN REVIEWED AND IS APPROVED FOR PUBLICATION IN ACCORDANCE WITH ASSIGNED DISTRIBUTION STATEMENT.

//Signature//

PATRICK CARLIN, Project Engineer
Composite Materials and Processing Section
Composite Branch
Structural Materials Division

//Signature//

DANIEL J. EVANS, Chief
Metals Branch
Structural Materials Division

//Signature//

ROBERT T. MARSHALL, Deputy Chief
Structural Materials Division
Materials And Manufacturing Directorate

This report is published in the interest of scientific and technical information exchange, and its publication does not constitute the Government's approval or disapproval of its ideas or findings.

1.0 REPORT DOCUMENTATION PAGE			<i>Form Approved</i> OMB No. 0704-0188	
<small>The public reporting burden for this collection of information is estimated to average 1 hour per response, including the time for reviewing instructions, searching existing data sources, gathering and maintaining the data needed, and completing and reviewing the collection of information. Send comments regarding this burden estimate or any other aspect of this collection of information, including suggestions for reducing this burden, to Department of Defense, Washington Headquarters Services, Directorate for Information Operations and Reports (0704-0188), 1215 Jefferson Davis Highway, Suite 1204, Arlington, VA 22202-4302. Respondents should be aware that notwithstanding any other provision of law, no person shall be subject to any penalty for failing to comply with a collection of information if it does not display a currently valid OMB control number. PLEASE DO NOT RETURN YOUR FORM TO THE ABOVE ADDRESS.</small>				
1. REPORT DATE (DD-MM-YY) October 2015		2. REPORT TYPE Final		3. DATES COVERED (From - To) 23 July 2013 - 21 September 2015
4. TITLE AND SUBTITLE METALLIC AND CERAMIC MATERIALS RESEARCH Task Order 0003: Metallic Materials, Processing and Performance Development for Air Force Applications			5a. CONTRACT NUMBER FA8650-10-D-5226-0003	
			5b. GRANT NUMBER	
			5c. PROGRAM ELEMENT NUMBER 62102F	
6. AUTHOR(S) Sang-Lan Kim, David S. Lee, Triplicane A Parthasarathy, Satish I. Rao, Oleg N. Senkov, James M. Scott, and Vikas Sinha			5d. PROJECT NUMBER 4347	
			5e. TASK NUMBER	
			5f. WORK UNIT NUMBER X0LX	
7. PERFORMING ORGANIZATION NAME(S) AND ADDRESS(ES) UES, Inc. 4401 Dayton Xenia Rd Dayton, OH 45432			8. PERFORMING ORGANIZATION REPORT NUMBER	
9. SPONSORING/MONITORING AGENCY NAME(S) AND ADDRESS(ES) Air Force Research Laboratory Materials and Manufacturing Directorate Wright-Patterson Air Force Base, OH 45433-7750 Air Force Materiel Command United States Air Force			10. SPONSORING/MONITORING AGENCY ACRONYM(S) AFRL/RXCCM	
			11. SPONSORING/MONITORING AGENCY REPORT NUMBER(S) AFRL-RX-WP-TR-2016-0012	
12. DISTRIBUTION/AVAILABILITY STATEMENT Distribution Statement A. Approved for public release; distribution unlimited.				
13. SUPPLEMENTARY NOTES PA Case Number: 88ABW-2015-6172; Clearance Date: 22 Dec 2015. This report contains color.				
14. ABSTRACT (Maximum 200 words) This final report details progress made on various topics related to advanced metallic and advanced metallic composites. In this program, the work covered the material needs for enabling a variety of missions including access to space and hypersonic flight for global access and meeting the continuing demand for higher performance, more efficient jet engines. The focus areas covered a broad range of technologies comprising thermal protection materials, fiber lasers for directed energy, Integrated Computational Materials Science and Engineering (ICMSE), superalloy development, hybrid disks, hot structures for hypersonics, functional materials for energy needs, and nanoenergetic materials for munitions needs. This report will cover three categories of research: advanced ceramics/composites, advanced metals, and functional metals. Much of this research has been published elsewhere in the open literature as journal articles and papers, and is referenced in the text.				
15. SUBJECT TERMS high entropy alloys, titanium, inertia welding				
16. SECURITY CLASSIFICATION OF:			17. LIMITATION OF ABSTRACT: SAR	18. NUMBER OF PAGES 37
a. REPORT Unclassified	b. ABSTRACT Unclassified	c. THIS PAGE Unclassified		
				19b. TELEPHONE NUMBER (Include Area Code) 937-904-5547

Table of Contents

Table of Contents	1
List of Figures	ii
List of Tables	iv
Forward	v
1.0 Executive Summary	1
2.0 Task Order 0003 – Advanced Metals Research.....	2
2.1 Integrated Computational Materials Science and Engineering (ICMSE)	2
2.1.1 Screw Dislocation Cross-slip Induced Dipole Annihilation in FCC	2
2.1.2 Microstructure-Sensitive Design Tool for Strain Rate Sensitive Flow Stress	3
2.2 Alloy Development and Discovery	5
2.2.1 High Entropy Alloys	5
2.2.2 Amorphous Metallic Alloys.....	15
2.3 Alloy Processing and Characterization	18
2.3.1 Solid State Joining	18
2.3.2 Characterization of γ' Precipitates in Ni-based Superalloys.....	21
2.4 Alloy Processing and Characterization	21
2.4.1 Thermal Transport in Copper/Diamond System.....	21
References.....	25
List of Acronyms	27

List of Figures

Figure 1: Critical Escaig stresses on the glide plane required for the annihilation of two oppositely-signed jogged $\frac{1}{2}\langle 1-10 \rangle$ screw dislocations separated by 14 and 44 nm on the [1 1-1] cross-slip plane, as a function of temperature. Also shown are the critical Escaig stress on the cross-slip plane and critical glide stress on the cross-slip plane for the jogged screw dislocation annihilation process at 5 K.....	3
Figure 2: The quality of prediction versus experimental data is shown for the fast acting model derived for LSHR alloy: (a) the yield stress and (b) creep stress along with yield stress.	4
Figure 3: Effect of Statistical Variability in the Microstructure of IN100 Alloy on the Resolved Shear Stress Predicted using 2D DD model.	5
Figure 4: X-ray diffraction patterns from the cast and homogenized refractory HEAs: (a) NbTiVZr (BCC phase), (b) NbTiV ₂ Zr (3 BCC phases), (c) CrNbTiZr (BCC and Laves phases) and (d) CrNbTiVZr (BCC and Laves phases).	7
Figure 5: (a) Three phases: BCC1 (bright color dendrites), BCC2 (grey color interdendrites) and Laves C15 (dark color particles inside BCC2) in the as-cast CrMo _{0.5} NbTa _{0.5} TiZr. (b) Calculated solidification curve showing the sequence of formation of the three phases and eutectic origin of BCC2 and Laves phases.....	10
Figure 6: Temperature dependences of the specific yield strength of refractory-based high entropy alloys and three Ni-based superalloys.	11
Figure 7: (a) Most frequent phases in screened HEAs at solidus temperature (T_m) and 600 °C. (b) Fraction of HEAs containing only SS phases at T_m and 600 °C. CALPHAD.	14
Figure 8: Ashby plots showing (a) maximum use temperature vs. alloy density and (b) Young's modulus vs. alloy density for 3-, 4-, 5-, and 6- component equiatomic SS alloys. Note that the range of the properties narrows with an increase in the number of components. For example, only few 6-component alloys have $T_{use} > 1000$ °C and density below 6 g/cm ³ , while there is a number of 3- and 4-component alloys satisfying these requirements.....	15
Figure 9: (a) Experimental (solid lines) and QMD-simulated (dashed lines) total radial distribution functions, $G(r)$, of Ca-Mg-Zn and Ca-Mg-Cu amorphous alloys. (b) QMD-simulated partial radial distribution functions, $g_{ij}(r)$, for Ca ₆₀ Mg ₁₅ Zn ₂₅	16
Figure 10: (a) The most prevalent clusters by Voronoi index and (b) average size and number of networks of icosahedral clusters in a Cu _{64.3} Zr _{35.7} metallic glass as a function of temperature during a quench at 1011 K/s. The most prevalent clusters during cooling for (c) Cu ₇₀ Zr ₃₀ and (d) Cu ₃₀ Zr ₇₀ are also shown.	18
Figure 11: (a) Backscatter electron image and (b) inverse pole figure map of the IFW region showing transition from a flat (right) to wavy (left) weld interface appearance. The weld interface is outlined by a white line in figure (b). The LSHR alloy is below the IFW interface and it is darker than the Mar-M247 alloy in figure (a).	20

Figure 12: (a) True (f') and (b) imaginary (f'') parts of the X-ray scattering factors for Al, Co, Cr, Mo, Nb, Ni, and Ti in the X-ray energy range of 5000–25000 eV. The vertical lines correspond to the energies used in this work..... 21

Figure 13: SIMS depth profiles showing nitrogen concentration as a function of depth below the surface for synthetic and natural diamond substrates. 23

Figure 14: Effect of Ti Interface Layer Thickness on Cu/Diamond Interface Thermal Conductance. The solid lines depict the approximate trend for experimental data points. The dotted horizontal lines depict the predictions of acoustic mismatch and diffuse mismatch models (AMM and DMM) for Cu/diamond interface..... 24

List of Tables

Table 1: High throughput screening and evaluation of structural HEAs.....	13
---	----

Forward

This report was prepared by the Materials and Processes Division of UES, Inc., Dayton, Ohio under Air Force Contract No. FA8650-10-D-5226. Mr. Patrick Carlin and Lt. Andrew Nauss of the Structural Materials Division of the Air Force Research Laboratory were the Government Project Engineers. The research reported herein covers the period 1 October 2013 through 21 September 2015.

2.0 Executive Summary

The materials research and development program for the Air Force is largely driven by the perceived needs of high level initiatives such as Versatile Affordable Advanced Turbine Engine (VAATE), Integrated High Performance Rocket Propulsion Technology (IHDRPT), Adaptive Versatile Engine Technology (ADVENT), Integrated Vehicle Energy Technology (INVENT), X-51 Scramjet Engine Demonstrator, and Highly Efficient Embedded Turbine Engine (HEETE). Factors such as the material temperature, design stress, thermal stability, distortion tolerance, expected design life, and environmental resistance requirements vary significantly between these initiatives, between requirements of the eventual weapon systems, and between various components within them. The limiting/enabling properties also vary significantly. Thus there is a need to invest in Research and Development (R&D) on a variety of materials with a breadth sufficient to facilitate eventual optimization of specific property sets that are application specific. Since funding limitations restrict the exploration space, and since there is a need to accelerate the development and transition of advanced materials in a timely manner, computational materials science and engineering is essential.

In this program, the work covered the material needs for enabling a variety of missions including access to space and hypersonic flight for global access and meeting the continuing demand for higher performance, more efficient jet engines. The focus areas covered a broad range of technologies comprising ceramic composites, thermal protection materials, fiber lasers for directed energy, Integrated Computational Materials Science and Engineering (ICMSE), superalloy development, hybrid disks, hot structures for hypersonics, functional materials for energy needs, and nanoenergetic materials for munitions needs. This report will cover two categories of research, advanced metals and functional metals.

3.0 Task Order 0003 – Advanced Metals Research

3.1 Integrated Computational Materials Science and Engineering (ICMSE)

3.1.1 Screw Dislocation Cross-slip Induced Dipole Annihilation in FCC

Cross-slip of screw character dislocations is an elementary, thermally-activated mechanism that is all prevalent in plastic deformation. The consequences of cross slip are recognized as the most important single process underlying complex spatiotemporal development of dislocation microstructure leading to hardening, pattern formation, and dynamic recovery. The early work of Escaig remains the most widely cited and used model for cross-slip; however, this model poses several difficulties with respect to quantitative simulations. Previously, atomistic simulations (molecular statics) were used with embedded atom potentials to evaluate the activation barrier for a screw dislocation to transform from fully residing on the glide plane to fully residing on the cross-slip plane, where the screw dislocation was intersecting a mildly-attractive 120° forest dislocation forming Glide locks (GL), Lomer–Cottrell (LC) locks, or Hirth locks, in both Ni and Cu. The cross-slip process was also explored at mildly-repulsive screw dislocation intersections. In these simulations, the Burgers vector of the intersecting dislocation forming mildly attractive GL or LC locks was reversed. The activation energies at attractive intersections were computed using two different techniques: (a) determine the equilibrium configurations (energies) when varying pure tensile or compressive stresses that are applied along the $[111]$ direction on the partially cross-slipped state, and (b) the classical nudged elastic band method. The cross-slip activation energies at the attractive intersections were found to be a factor of 3–20 lower than the energy for cross-slip at an isolated screw dislocation. At mildly repulsive intersections, cross-slip nucleation was found to be spontaneous and athermal, with zero cross-slip activation energy. These findings provide a better physical basis to represent local cross-slip processes in larger-scale, discrete dislocation-dynamics simulations, enabling more realistic simulations of the evolution of the dislocation substructure. Such simulations should result in improved statistical representation of cross-slip effects during monotonic or cyclic deformation.

In this study, cross-slip nucleation is examined at atomic jogs on screw dislocations using Mishin’s interatomic potentials for Ni and Cu, which give elastic constants and stacking fault energies close to experimental values [1]. The line direction of the jog resides on the cross-slip plane. It is argued that all types of atomic jogs on screw dislocation can be decomposed into a jog on a cross-slip plane plus a kink on the glide plane. Therefore, we have only considered one type of atomic jog on a cross-slip plane for calculating the cross-slip activation energy, as well as for the screw-dipole annihilation simulations. The annihilation of jogged-screw dipoles having initial separations of 14 and 44 nm were also simulated. The critical Escaig stresses for cross-slip nucleation and screw dipole annihilation, as a function of temperature, were determined using molecular dynamics simulations.

Large-scale atomistic simulations were used to examine the effect of jogs on the cross-slip of screw dislocations and screw dipole annihilation in Cu and Ni. Results are summarized in Figure 1. From these simulations, the following conclusions are drawn:

- (1) The stress-free activation energy for cross-slip of screw dislocations at jogs is approximately 0.4 eV in FCC Cu and Ni; a factor of 4–5 lower than the activation energy for cross-slip of screw dislocations in the absence of a jog.

- (2) The critical Escaig stress on the glide plane for jogged screw dipole annihilation drops from the 0 K value of 400 MPa to 0 MPa at room temperature and dipole annihilation is nearly athermal at room temperature.
- (3) At 5 K, Escaig stresses on the cross-slip plane are a factor of 1.5 less effective than Escaig stresses on the glide plane and glide stresses on the cross-slip plane are a factor of 3 less effective for dipole annihilation by cross-slip.
- (4) The activation volume for cross-slip of screw dislocations at jogs with respect to these three stress components range from 6 to 20 b^3 .

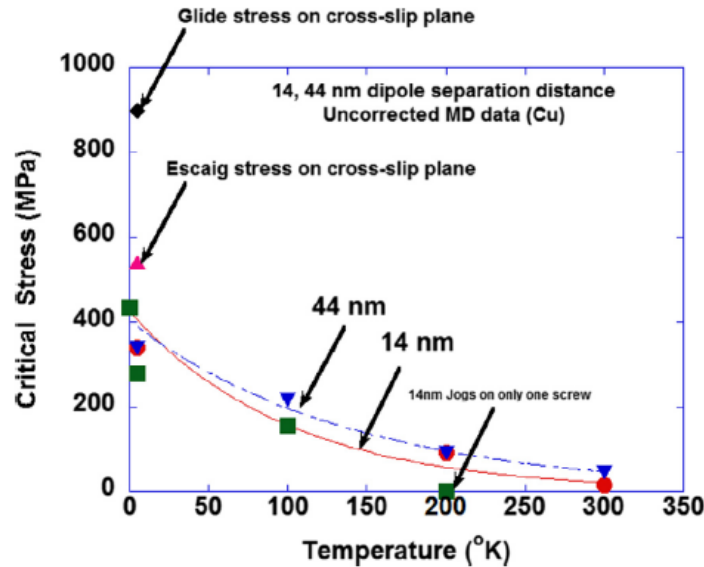


Figure 1: Critical Escaig stresses on the glide plane required for the annihilation of two oppositely-signed jogged $\frac{1}{2}\langle 1-10 \rangle$ screw dislocations separated by 14 and 44 nm on the $[1\ 1-1]$ cross-slip plane, as a function of temperature. Also shown are the critical Escaig stress on the cross-slip plane and critical glide stress on the cross-slip plane for the jogged screw dislocation annihilation process at 5 K.

These results, along with previously published simulation results on intersection cross-slip nucleation in FCC crystals, have been found useful in physics-based modeling of cross-slip in higher length scale, 3D dislocation dynamics simulations that have investigated dislocation pattern formation and fatigue structures in FCC crystals.

3.1.2 Microstructure-Sensitive Design Tool for Strain Rate Sensitive Flow Stress

A physics-based microstructure-sensitive design tool that predicts the flow stress of a low solvus high refractory (LSHR) alloy was developed. The thermally activated component of the yield model was obtained by including a yield stress dependent creep model formulated originally by Wilshire et al. [2], and by invoking a temperature dependent anti-phase boundary (APB) energy based on a formalism that captures high temperature order parameter of Ni_3Al . The resultant model was found to capture experimental data on all reported data on dual heat treated LSHR, including the standard subsolvus and supersolvus conditions. A microstructural evolution model, developed by Dr. Semiatin (AFRL/RX), was then integrated with the yield model to show that it

was possible to predict the evolution of strain rate dependent flow stress as a function of temperature from the thermal history of the alloy.

Figure 2 shows a comparison of the predictions with experimental data for yield stress and creep stress for the LSHR alloy. The data were taken from the work included in a NASA tech report [3]. It is seen that all of the yield data is captured by the model. For creep, the model captures the behavior of the large grained supersolvus alloy, but not the fine grained subsolvus. Future work will include this grain size effect.

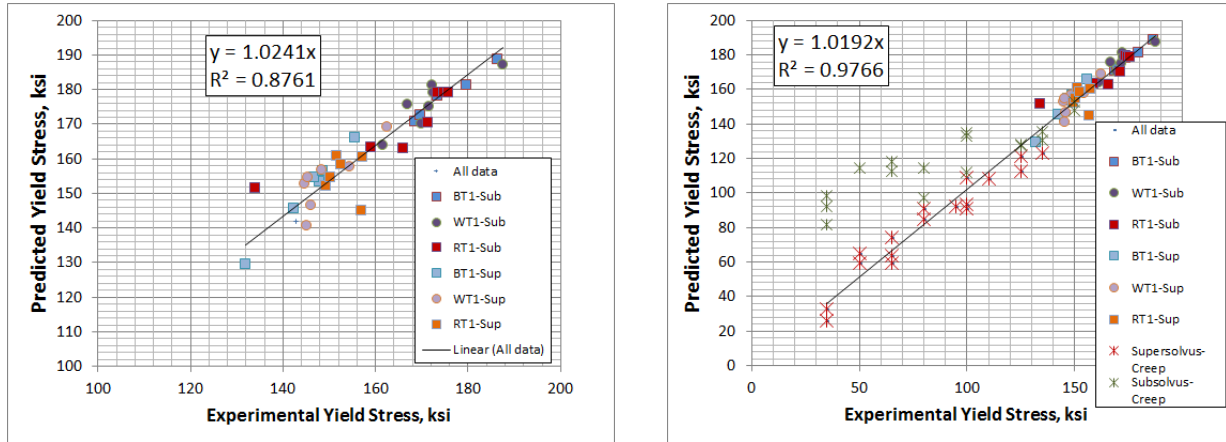


Figure 2: The quality of prediction versus experimental data is shown for the fast acting model derived for LSHR alloy: (a) the yield stress and (b) creep stress along with yield stress.

To assess the sensitivity of the discrete dislocation (DD) model to microstructural variations, an IN100 alloy microstructure, obtained by a custom heat treatment (Dr. J. Tiley, AFRL/RXCM) was chosen. The microstructures were segmented and divided into 3 x 3, 6 x 6 and 12 x 12 micron sections by Dr. M. Uchic (AFRL/RX). These images were used, along with the DD model, to obtain the effect of microstructural sampling size and variability. In Figure 3, the effect of sampling size on the predicted resolved stress in the case of IN100 is shown; as the sample size increases, the scatter in the data reduces. The mild increase in resolved shear stress was unexpected, but the key effect of reduction in scatter with increasing sampling size is as expected.

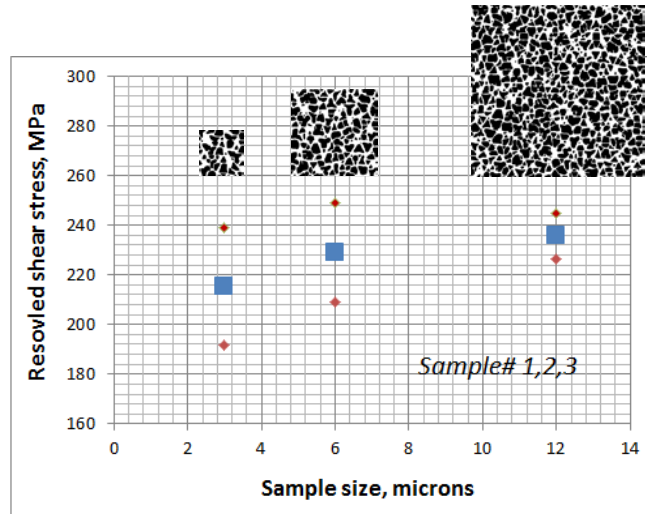


Figure 3: Effect of Statistical Variability in the Microstructure of IN100 Alloy on the Resolved Shear Stress Predicted using 2D DD model.

3.2 Alloy Development and Discovery

3.2.1 High Entropy Alloys

3.2.1.1 Low-density Refractory High-entropy Alloys of the Cr-Nb-Ti-V-Zr System

In the preceding reporting period, we used an advanced high entropy alloy (HEA) approach to produce several new refractory alloys with promising combinations of room temperature and elevated temperature mechanical properties and oxidation resistance. These are MoNbTaW, MoNbTaVW, HfNbTaTiZr, and CrMo_{0.5}NbTa_{0.5}TiZr. The high entropy of mixing and similar atomic radii of the alloying elements resulted in the formation of a single-phase body centered cubic (BCC) crystal structure in the first three alloys. However, the presence of Cr with an atomic radius that is much smaller than the atomic radii of other elements in the fourth alloy caused the additional formation of a minor fcc Laves phase. These refractory alloys have rather high densities, from 8.2 g/cm³ for CrMo_{0.5}NbTa_{0.5}TiZr to 13.8 g/cm³ for MoNbTaW, which may be satisfactory for potential applications of stationary structures that do not suffer from high weight. Since the aerospace industry demands low-density metallic alloys for high-temperature load-bearing structures and thermal protection systems, there is a clear rationale for exploring HEAs composed of constituents with high melting temperatures and reduced densities.

Therefore, the goal of the current work was to produce refractory HEAs with densities below 7.0 g/cm³, which could operate at temperatures as high as 1000 °C. To achieve this goal, low-density refractory elements, V ($\rho = 6.11 \text{ g/cm}^3$), Zr ($\rho = 6.51 \text{ g/cm}^3$), Cr ($\rho = 7.14 \text{ g/cm}^3$), Nb ($\rho = 8.57 \text{ g/cm}^3$), and Ti ($\rho = 4.51 \text{ g/cm}^3$) were selected to produce four alloys: NbTiVZr, NbTiV₂Zr, CrNbTiZr, and CrNbTiVZr. The microstructure, phase compositions and mechanical properties of these alloys have been studied and reported in two technical papers [4, 5].

Microstructure and phase analysis. The produced NbTiVZr, NbTiV₂Zr, CrNbTiZr, and CrNbTiVZr alloys have densities of 6.52, 6.34, 6.67, and 6.57 g/cm³, respectively, and are more than 20% lighter than Ni-based superalloys. Disordered BCC solid solution phases are the major phases in these alloys, and Cr-containing alloys additionally contain an ordered Laves phase

(Figure 4). Non-equilibrium and equilibrium phase diagrams have been modeled for the studied alloys via extrapolation of the interaction parameters from the lower order constituent binary and ternary systems to higher order interactions. The models show that, after non-equilibrium solidification, the NbTiVZr and NbTiV₂Zr alloys are essentially single-phase disordered BCC structures containing less than 1% of the secondary BCC phase. The disordered BCC phase also dominates (>91%) in the Cr-containing alloys, which additionally contain a Laves phase based on Cr and Zr. Thermodynamic modeling of equilibrium phases shows that all of the alloys have a single-phase BCC disordered structure (A2-1) just below their solidus temperature. The temperature range of stability of this phase is greatest in the NbTiVZr alloy (down to 726 °C), followed by the NbTiV₂Zr alloy (down to 843 °C). At lower temperatures, the A2-1 phase is predicted to partially transform in the secondary BCC (A2-2) and hexagonal phases in these alloys.

The Cr-containing alloys also show the presence of a Laves phase below 1363 and 1234 °C for the CrNbTiZr and CrNbTiVZr alloys, respectively. Comparing the thermodynamic modeling with experimental results shows that the volume fractions and compositions of the BCC phases identified in the studied alloys at room temperature approximately correspond to the equilibrium fractions and compositions of these phases at temperatures of ~600–750 °C. The present work thus suggests that the cooling rate of 10 °C/min used to chill the alloys after homogenization treatment at 1200 °C is too rapid to achieve equilibrium conditions below 600–750 °C. Thermodynamic databases based on the binary and ternary systems are able to predict correct trends, but are unable to accurately predict volume fractions and compositions of the Laves phases in the CrNbTiZr and CrNbTiVZr alloys. Although the stabilization of disordered solid solutions is the defining feature of high entropy alloys, the present work identifies two systems where an ordered intermetallic (IM) phase is stable at room temperature and can be fully dissolved at high temperatures. This suggests a reasoned approach for developing high entropy alloys with both solid solution and ordered phases as candidate high-temperature structural materials [4].

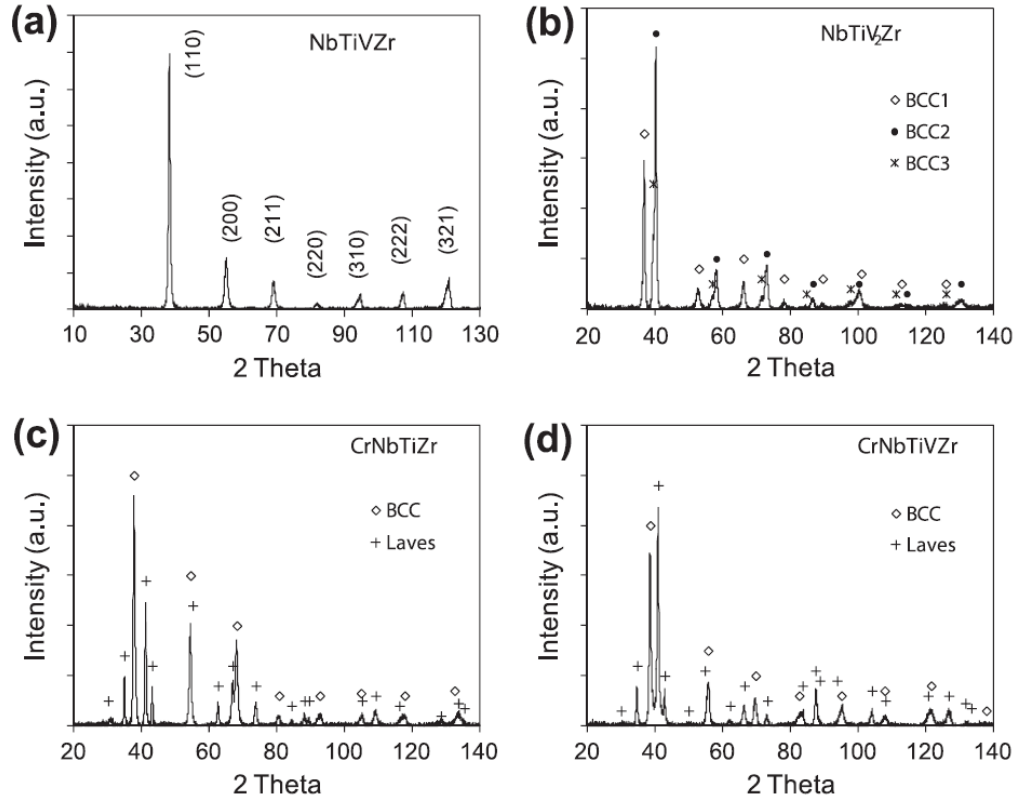


Figure 4: X-ray diffraction patterns from the cast and homogenized refractory HEAs: (a) NbTiVZr (BCC phase), (b) NbTiV₂Zr (3 BCC phases), (c) CrNbTiZr (BCC and Laves phases) and (d) CrNbTiVZr (BCC and Laves phases).

Mechanical properties. The produced NbTiVZr, NbTiV₂Zr, CrNbTiZr, and CrNbTiVZr alloys have Vickers microhardness values of 3.29, 2.99, 4.10, and 4.72 GPa, respectively, which is comparable with the hardness of high strength steels. The compression properties of the NbTiVZr, NbTiV₂Zr, CrNbTiZr, and CrNbTiVZr alloys were determined in the temperature range from 25 °C to 1000 °C. The NbTiVZr and NbTiV₂Zr alloys showed good compressive ductility at all studied temperatures while the Cr-containing alloys showed brittle-to-ductile transition occurring somewhere between 25 °C and 600 °C. Strong work hardening was observed in the NbTiVZr and NbTiV₂Zr alloys during deformation at room temperature. The alloys had yield strengths of 1105 MPa and 918 MPa, respectively, and their strength continuously increased, exceeding 2000 MPa after 40% compression strain. The CrNbTiZr and CrNbTiVZr alloys showed high yield strength (1260 MPa and 1298 MPa, respectively) but low ductility (6% and 3% compression strain, respectively, before the fracture) at room temperature.

Cleavage fracture of Laves phase particles and ductile fracture of the BCC phase was observed in these alloys. The fracture of these alloys was associated with extensive material fragmentation and local heating beyond the melting temperature. Strain softening and steady state flow were typical during compression deformation of these alloys at temperatures above 600 °C. In these conditions, the alloys survived 50% compression strain without fracture and their yield strength continuously decreased with an increase in temperature. During deformation at 1000 °C, the NbTiVZr, NbTiV₂Zr, CrNbTiZr, and CrNbTiVZr alloys showed yield strengths of 58 MPa, 72 MPa, 115 MPa, and 259 MPa, respectively. During deformation at 1000 °C, the NbTiVZr and

NbTiV₂Zr alloys had a single-phase BCC structure. After deformation at 1000 °C followed by cooling to room temperature, the phase compositions of the NbTiVZr and NbTiV₂Zr alloys noticeably changed relative to the respective homogenized conditions. In addition to the matrix phase, two additional BCC phases were observed in NbTiVZr, predominantly inside the deformation bands. In NbTiV₂Zr, the volume fraction of one of the three BCC phases observed after homogenization treatment considerably reduced after deformation. It is suggested that the high density of dislocations and subgrain boundaries in the deformed alloys facilitates transformation of the high-temperature BCC phase into the low-temperature BCC phase during cooling after deformation.

The results indicate that the phases present in these two alloys at room temperature are likely metastable phases, which are quenched from higher temperatures due to slow diffusion kinetics of the alloying elements. During deformation at 1000 °C, the CrNbTiZr, and CrNbTiVZr alloys retained their two phase (BCC plus Laves) structure and their phase compositions were unaffected by deformation. The high temperature deformation resulted in the formation of new recrystallized grains inside the BCC phase and deformation twins inside large Laves-phase particles. The CrNbTiVZr alloy showed the most attractive properties, such as considerably improved elevated temperature strength, reduced density and much higher melting point, as compared to three other high entropy alloys and referenced Ni superalloys (In718 and Haynes 230). A microstructural approach to improve the limited room temperature ductility is suggested via dissolution and controlled precipitation of the strengthening Laves phase [5].

3.2.1.2 Phase Composition of a CrMo_{0.5}NbTa_{0.5}TiZr High Entropy Alloy

The design and development of HEAs is built upon the fact that high configuration entropy makes a significant contribution to the phase stability of random mixed disordered solution phases. However, the stability of a phase is determined by its Gibbs energy, which includes contributions from both enthalpy and entropy. The microstructure of an alloy is therefore the result of stability competition among a variety of phases in the system. Phase diagrams, which are considered the road maps for materials design, provide essential information on the phase stability at a given alloy chemistry and temperature. While most of the binary phase diagrams and some ternary sections have been determined via experimental approach, and they can be found in the literature and handbooks, this is not the case for multi-component systems. Determination of multi-component phase diagrams solely by experimental approaches is obviously not feasible due to the tremendous amount of work involved.

In recent years, integration of the calculation of phase diagrams (CALPHAD) approach with key experiments has been used as an effective approach in the determination of complicated multi-component phase diagrams. The essence of the CALPHAD approach is to develop a thermodynamic database for a multi-component system using experimental data from the constituent binaries and ternaries. This database is then used to calculate the phase stability of the multi-component system. The CALPHAD approach has been successfully applied to the design of traditional alloys based on one key element. In this case, the thermodynamic database needs to be validated only at the corner of the key element. At the same time, to successfully design HEAs that are based on several multiple principal elements, the multi-component thermodynamic database must be developed and validated for the entire composition space, which is a very challenging task. In this work, a thorough analysis of the microstructure, phase

composition and chemical composition of phases in a $\text{CrMo}_{0.5}\text{NbTa}_{0.5}\text{TiZr}$ refractory high entropy alloy was conducted in as-solidified and annealed conditions. The experimental results were compared with the results of solidification and phase equilibrium simulations conducted for this alloy. The purpose of this study was to see if a currently available extensive thermodynamic database can predict the correct topology of phase equilibria in the multi-principal component alloy and to understand the limitations of this database for use in the design of HEAs.

The microstructure and phase composition of a $\text{CrMo}_{0.5}\text{NbTa}_{0.5}\text{TiZr}$ high entropy alloy were studied in the as-solidified condition and after heat treatment at 1450 °C for 3 h and 1000 °C for 100 h [6]. In the as-solidified condition, the alloy consists of three phases, two of which have disordered BCC crystal structures and the third has an ordered cubic Laves phase (Figure 5a). The BCC1 phase solidifies first in the form of dendrites enriched with high-melting-temperature elements, Mo, Ta, and Nb, and its volume fraction is 42%. The BCC2 and Laves phases likely solidify by eutectic-type reaction filling inter-dendritic regions. The volume fractions of these phases are 27% and 31%, respectively. The BCC2 phase is enriched with Ti and Zr, and the Laves phase is heavily enriched with Cr and slightly with Zr. In addition to Cr and Zr, the Laves phase also contains other alloying elements, with the total amount of 37.1%. Hot isostatic pressing (HIP) at 1450 °C for 3 h results in coagulation of the BCC1 dendrites into round-shaped particles and in an increase in the volume fraction of the BCC1 phase to 67%. The volume fractions of the BCC2 and Laves phases decrease to 16% and 17%, respectively. These volume fraction changes cause re-distributions of the alloying elements between the phases. For example, the concentration of Cr in the BCC1 phase increases and in the BCC2 phase decreases. However, the main tendency observed for the as-solidified condition remains: the BCC1 phase remains enriched with Mo, Nb, and Ta, the BCC2 phase is enriched with Ti and Zr and the Laves phase is enriched with Cr. Annealing at 1000 °C for 100 h, conducted after the HIP processing, results in precipitation of fine, submicron-sized Laves particles inside the BCC1 phase, which causes a decrease in the concentration of Cr and Ta in the BCC1 phase and a decrease in the volume fraction of this phase. After annealing, the alloy consists of 52% BCC1, 16% BCC2 and 32% Laves phases. Thermodynamic analyses of the solidification process and phase equilibria in the $\text{CrMo}_{0.5}\text{NbTa}_{0.5}\text{TiZr}$ alloy were carried out using the thermodynamic database developed by the CALPHAD approach. The Scheil solidification model correctly predicts formation of 3 identified phases, two of which (BCC2 and Laves) likely form by eutectic reaction (Figure 5b).

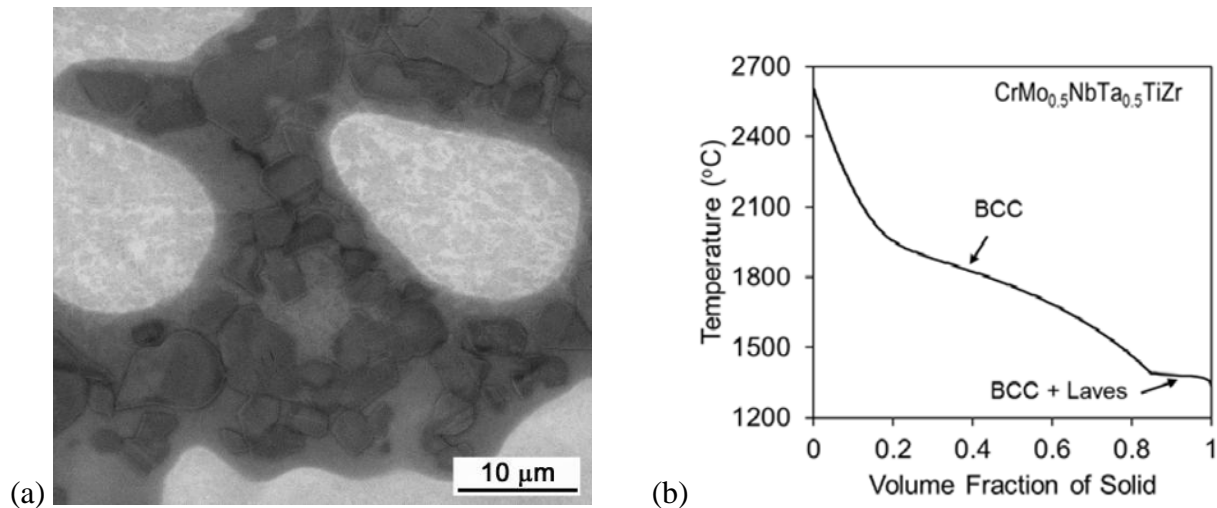


Figure 5: (a) Three phases: BCC1 (bright color dendrites), BCC2 (grey color interdendrites) and Laves C15 (dark color particles inside BCC2) in the as-cast $\text{CrMo}_{0.5}\text{NbTa}_{0.5}\text{TiZr}$. (b) Calculated solidification curve showing the sequence of formation of the three phases and eutectic origin of BCC2 and Laves phases.

3.2.1.3 Development of Low-density Refractory-based HEAs Containing Aluminum

In this work, Al was added to several earlier developed refractory HEAs to reduce alloy density, increase high temperature strength and specific strength, and improve oxidation resistance. An additional objective of this work was to study whether Al additions stimulate or suppress formation of IM phases in refractory HEAs. All reported refractory HEAs that do not contain Cr are BCC structures, whereas alloys with Cr contain Laves phases and have a considerably decreased ductility at temperatures below 800 °C. The introduction of the Laves phases seems to be associated with the atomic radius of Cr ($r_{\text{Cr}} = 128$ pm), which is much smaller than that of other refractory elements (~ 146 pm). Although Al forms a number of IM phases with transition elements in conventional alloys, it favors the formation of disordered BCC phases in Co-Cr-Fe-Ni-based HEAs. It is worth noting that the atomic radius of Al ($r_{\text{Al}} = 143$ pm) is similar to the atomic radii of refractory elements. One may therefore expect that the addition of Al may impede formation of IM phases in HEAs that do not contain Cr and thus may improve ductility.

Six new refractory HEAs have been produced by arc melting and their phase composition, microstructure, and properties have been studied [7]. In addition to the refractory elements, the alloys also contain Al and Ti, which reduce the alloy density. Three alloys, $\text{AlMo}_{0.5}\text{NbTa}_{0.5}\text{TiZr}$ (A1), $\text{Al}_{0.3}\text{NbTaTi}_{1.4}\text{Zr}_{1.3}$ (A4), and $\text{Al}_{0.5}\text{NbTa}_{0.8}\text{Ti}_{1.5}\text{V}_{0.2}\text{Zr}$ (A6) contain two BCC phases with very similar lattice parameters. Both phases are present in the form of interpenetrating nanolamellae creating basket-weave nanostructure inside grains. One phase is enriched with Nb and another phase is enriched with Zr. The densities of these alloys are 7.4 g/cm^3 (A1), 8.2 g/cm^3 (A4), and 7.4 g/cm^3 (A6), and their Vickers hardness values are 5.8 GPa, 4.8 GPa, and 5.2 GPa, respectively. Three other alloys, $\text{AlNb}_{1.5}\text{Ta}_{0.5}\text{Ti}_{1.5}\text{Zr}_{0.5}$ (A2), $\text{Al}_{0.4}\text{Hf}_{0.6}\text{NbTaTiZr}$ (A3), and $\text{Al}_{0.3}\text{NbTa}_{0.8}\text{Ti}_{1.4}\text{V}_{0.2}\text{Zr}_{1.3}$ (A5) are essentially single-phase BCC alloys. However, nanometer-sized secondary phases are present at grain boundaries. The densities of these alloys are 6.9 g/cm^3 (A2), 9.0 g/cm^3 (A3), and 7.8 g/cm^3 (A5), and their Vickers hardness values are 4.0 GPa,

4.9 GPa, and 4.9 GPa, respectively. Compression tests reveal very high strengths for some of the studied alloys in the temperature range from 23 °C to 1200 °C, superior to the tensile strengths Ni-based superalloys, such as Inconel 718 and Mar-M247 (Figure 6). Compressive ductility is limited at 23 °C, suggesting that little or no tensile ductility may result at this temperature.

The properties of two new alloys, $\text{AlMo}_{0.5}\text{NbTa}_{0.5}\text{TiZr}$ and $\text{Al}_{0.4}\text{Hf}_{0.6}\text{NbTaTiZr}$ were compared with the properties of the parent $\text{CrMo}_{0.5}\text{NbTa}_{0.5}\text{TiZr}$ and HfNbTaTiZr alloys and the beneficial effects from the Al additions on the microstructure and properties were outlined [8]. In particular, complete substitution of Cr with Al in the $\text{CrMo}_{0.5}\text{NbTa}_{0.5}\text{TiZr}$ alloy reduced the alloy density by 10.1%, increased room temperature hardness and yield strength by ~12%, noticeably improved RT ductility and also considerably increased, by more than 50%, high-temperature strength in the temperature range from 800 °C to 1200 °C. These improvements in the mechanical properties were related to dramatic changes in the phase composition and microstructure. While the $\text{CrMo}_{0.5}\text{NbTa}_{0.5}\text{TiZr}$ alloy contained three relatively coarse phases, BCC1, BCC2, and Laves, only two BCC phases, mainly in the form of spinodal-like nano-lamellar structure, and no IM phases, were present in the $\text{AlMo}_{0.5}\text{NbTa}_{0.5}\text{TiZr}$ alloy. Partial substitution of Hf with Al in the HfNbTaTiZr alloy reduced the alloy density by ~9% and increased room temperature hardness and yield strength by 29% and 98%, respectively. The difference in the yield strength of the HfNbTaTiZr and $\text{Al}_{0.4}\text{Hf}_{0.6}\text{NbTaTiZr}$ alloys, however, rapidly disappears with an increase in temperature and the properties of these two alloys are the same at 1000 °C and 1200 °C. The temperature dependence of the specific yield strength of several refractory HEAs is superior to the properties of advance Ni-based superalloys (Figure 6). Moreover, due to their high melting points and strength, refractory HEAs can be used at much higher temperatures than Ni-based superalloys.

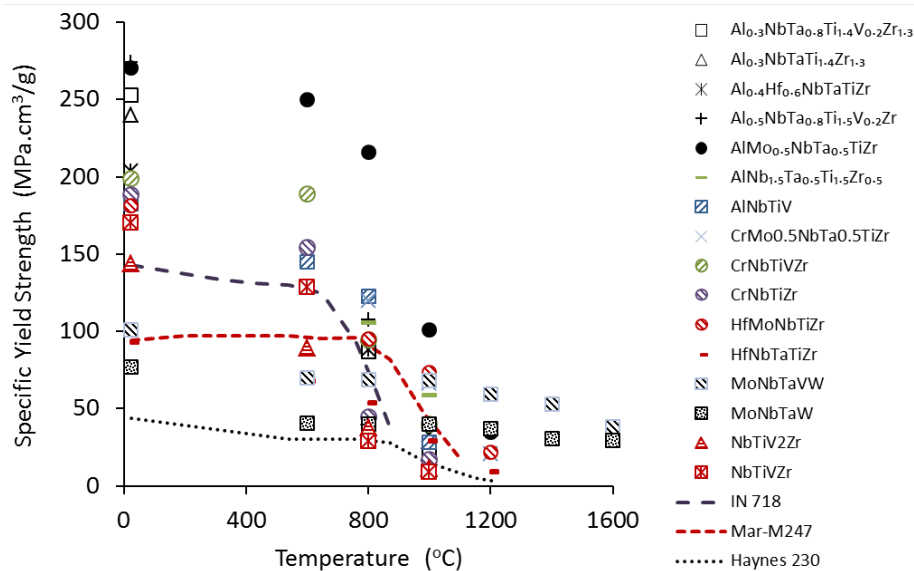


Figure 6: Temperature dependences of the specific yield strength of refractory-based high entropy alloys and three Ni-based superalloys.

3.2.1.4 Accelerated Exploration and Development of Multi-principal Element Alloys

Multi-principle element alloys (MPEAs, among which alloys with ≥ 5 elements are also called high entropy alloys, HEAs) are a new alloy development philosophy, where the base alloy has significant atom fractions of several elements. This new alloying strategy vastly increases the number of possible alloy systems, giving a rich composition and phase space that has not yet been explored. For example, a palette of 12 elements gives 12 conventional alloy systems where 1 element dominates. The same palette of 12 elements gives 495 alloy families with 4 base elements; 792 systems with 5 base elements, 924 6-base-element systems and a total of 4,017 alloy systems consisting of between 3 and 12 base elements. Thus, while the number of conventional alloy systems equals the number of elements in a palette, the number of MPEA systems is a function of $N!$, which vastly increases the number of systems. This greatly expands opportunities for discovering alloys with new and useful properties, but introduces a new challenge. It is relatively simple to choose an alloy system for an intended application when it is based on a single element - the properties of the base element are a useful guide for achieving target properties. But this is not so simple for MPEAs. Some properties such as density, elastic modulus, and cost can be reasonably estimated from the rule-of-mixtures of the base elements; however, this is not the case for important properties such as strength, ductility and maximum use temperature. Even simple experimental evaluations of these properties are time-intensive, requiring weeks or months to produce and characterize a small number of candidate alloys. Evaluating hundreds of thousands of candidates is a truly daunting task, requiring completely new approaches.

Exploration and Development of High Entropy Alloys for Structural Applications. We developed a strategy to design and evaluate high-entropy alloys (HEAs) for structural use in the transportation and energy industries [9]. We give HEA goal properties for low (≤ 150 °C), medium (≤ 450 °C), and high ($\geq 1,100$ °C) use temperatures. A systematic design approach uses palettes of elements chosen to meet target properties of each HEA family and gives methods to build HEAs from these palettes. We show that IM phases are consistent with HEA definitions, and the strategy developed here includes both single-phase, solid solution HEAs and HEAs with the intentional addition of a 2nd phase for particulate hardening. A thermodynamic estimate of the effectiveness of configurational entropy to suppress or delay compound formation is given. A 3-stage approach is given to systematically screen and evaluate a vast number of HEAs by integrating high-throughput computations and experiments (Table 1). CALPHAD methods are used to predict phase equilibria, and high-throughput experiments on materials libraries with controlled composition and microstructure gradients are suggested. Much of this evaluation can be done now, but key components (materials libraries with microstructure gradients and high-throughput tensile testing) are currently missing. Suggestions for future HEA efforts are given. More detailed information on the proposed strategy can be found in a published paper by Miracle, et. al. [9].

Table 1: High throughput screening and evaluation of structural HEAs

STAGE 0	High-Throughput CALPHAD Calculations of Phase Equilibria
	Use temperature (T_{use}) is less than the solidus temperature (T_{sol})
	Must have no 1st order phase transformation below T_{use}
	Must have 1 or 2 solid solutions or 1 solid solution plus 1 intermetallic phase at $T \leq T_{\text{use}}$
	Must be single phase solid solution at some temperature above T_{use}
	Phases are fcc, bcc, hcp or ordered derivatives
	Estimated σ must be at or below the critical
	Estimated E must be at or above the critical E
STAGE 1	High-Throughput Experiments Using Composition Gradients
	Measure phases present via EDS and EBSD mapping in SEM
	Measure phase transformations (including melting) via nano-calorimetry [62]
	Measure E via instrumented nano-indentation
	Measure strength capacity via instrumented nano-indentation or micro-pillar compression
	Measure capacity for plasticity via micro-pillar compression
	Measure capacity for oxidation resistance
	Refine the thermodynamic database using measured data
STAGE 2	High-Throughput Experiments Using Microstructure Gradients
	Measure tensile strength & ductility as function of temperature (<i>techniques not yet established</i>)

Accelerated Exploration of Multi-Principal Element Alloys with Solid Solution Phases. In this task, a fundamentally new combinatorial approach to rapidly screen a large number of candidate structural metal alloys using the CALPHAD method to calculate the phase diagram of each alloy has been established [10]. This gives a rudimentary microstructural assessment, since every calculated phase diagram gives the phases present and their reaction temperatures. Simple rules evaluate an alloy’s potential for structural applications. For example, the solidus temperature (T_m) must be above the maximum use temperature (T_{use}) and there should be no first-order phase transformations below T_{use} to avoid property changes during service. Good ductility and toughness are often associated with a solid solution primary phase, and the most potent strengthening mechanisms require the controlled distribution of a second phase. Typically, structural alloys are designed such that $T_{\text{use}} < T_s < T_m$, where T_s is the solvus temperature of the strengthening phase. The distribution and volume fraction of strengthening phases can be controlled by heat treatments above T_s , to dissolve the strengthening phase, followed by quenching and annealing between T_{use} and T_s to nucleate and grow the strengthening phase. Rules can also be applied regarding the number and types of phases and practical metrics such as alloy density, elastic properties, and alloy cost, which can be estimated by the rule of mixtures of the elements present. The developed approach has been applied to identify equiatomic alloys containing solid solution phases and a given set of thermodynamic and physical properties. We evaluate over 130,000 alloy systems, identifying promising compositions for more time-intensive experimental studies. The most frequent phases (over 60%) in the equiatomic alloys are three SS phases (BCC, FCC, A15, and HCP), silicides, B2 phase and Laves phases (Figure 7a). We find the surprising result that solid solution alloys become less likely as the number of alloy elements increases (Figure 7b). This contradicts the major premise of HEAs—that increased configurational entropy increases the stability of disordered solid solution phases. As the number of elements increases, the configurational entropy rises slowly while the probability of at least

one pair of elements favoring formation of IM compounds increases more rapidly, explaining this apparent contradiction.

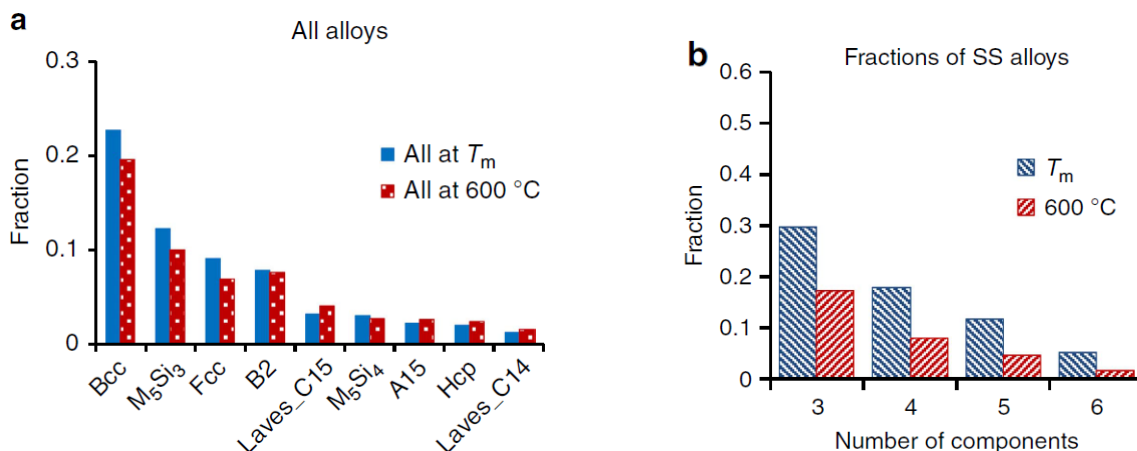


Figure 7: (a) Most frequent phases in screened HEAs at solidus temperature (T_m) and 600 °C. (b) Fraction of HEAs containing only SS phases at T_m and 600 °C. CALPHAD.

Accelerated Exploration of Multi-Principal Element Alloys for Structural Applications. In this task the strategy for accelerated discovery and exploration of multi-principal element alloys developed and reported in our two previous papers [9, 10] was used to identify new alloys within a design window of desired microstructures and properties [11]. As an example, the strategy was applied to analyze thousands of 3- 4-, 5-, and 6- component alloys at equiatomic compositions of the alloying elements. Currently available thermodynamic databases were used to assess equilibrium phase diagrams for these alloys. The validity and reliability of the calculated phase diagrams were estimated based on the extent of experimental binary and ternary data used to build the respective thermodynamic databases. Alloys with specific characteristics, such as single-phase solid solution alloys with the use temperature above 1000 °C, were identified using an automated analysis of the calculated phase diagrams. The density, elastic moduli, and costs of these alloys were estimated using the rule of mixtures of pure elements and were used as additional criteria for alloy selection (Figure 8). This approach allowed rapid, albeit preliminary, screening of many thousands of alloys and identification of promising candidate compositions, some of which are reported in this paper, for more time intensive experimental validations and assessments.

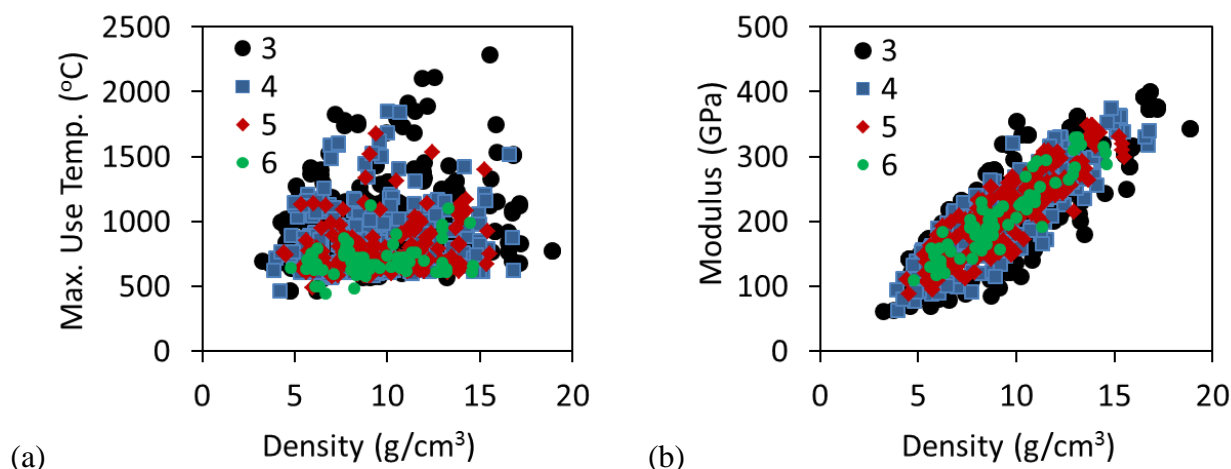


Figure 8: Ashby plots showing (a) maximum use temperature vs. alloy density and (b) Young's modulus vs. alloy density for 3-, 4-, 5-, and 6- component equiatomic SS alloys. Note that the range of the properties narrows with an increase in the number of components. For example, only few 6-component alloys have $T_{use} > 1000$ °C and density below 6 g/cm³, while there is a number of 3- and 4-component alloys satisfying these requirements.

3.2.2 Amorphous Metallic Alloys

3.2.2.1 Ab Initio MD Simulation of the Amorphous Structure of Ca-Mg-Cu-Zn Alloys

Structural analysis of metal-metal bulk metallic glasses (BMGs) is mainly focused on transition metal glasses such as Zr-Cu, Zr-Pt, and Zr-Cu-Al. The results indicate that the packing of atoms in these materials is not random, but is strongly influenced by chemical interactions. In particular, icosahedral short range order (SRO) has been identified and correlated to their good glass forming ability (GFA). On the other hand, the atomic structure of Ca-Mg-Zn BMGs, identified with the use of X-ray and neutron diffraction and Reverse Monte Carlo (RMC) simulation, shows no icosahedral SRO. Instead, five-fold bonds in the form of pentagonal bi-pyramids have been found to be the most populous structural units in these BMGs. A large fraction of five-fold bonds and the lack of icosahedral SRO has also been found in the molecular dynamic (MD) simulated amorphous structure of Mg-Cu alloys. In the present work, the atomic structures of several Ca-Mg-Cu and Ca-Mg-Zn BMGs were simulated with the use of ab initio (quantum) molecular dynamics (QMD) simulation. The simulated structures were then used to calculate partial (PRDF) and total (RDF) radial distribution functions, pair bond distances, and partial and total coordination numbers. The QMD-simulated results were validated through the experimentally determined RDFs.

The atomic structures of six Ca-Mg-TM ternary metallic glasses (TM is Cu or Zn) have been analyzed using neutron diffraction and ab initio molecular dynamics (QMD) modeling [12]. All six partial radial distribution functions (PRDFs), $g_{ij}(r)$, have been identified for each alloy. Figure 9a shows excellent agreement between the simulated and experimentally determined total radial distribution functions for the six studied alloys and Figure 9b shows QMD-simulated partial radial distribution functions, $g_{ij}(r)$, for Ca₆₀Mg₁₅Zn₂₅, as an example. It is found that the nearest-neighbor mode bond lengths are shorter than those in competing crystals. A noticeable

shortening of Ca-Cu, Mg-Cu, and Ca-Zn bond distances indicates strong interactions between these atom pairs, as supported by the calculated electronic structure. It is suggested that the bond shortening is enabled by the absence of long-range atomic order, which lowers the free energy of metallic glasses and increases GFA. Pronounced chemical short range ordering (CSRO) near TM atoms, chemical short range clustering (CSRC) near Ca atoms and a neutral environment near Mg atoms have been found. Increasing the Cu concentration from 15 to 35 at.% increases the total coordination number around Ca, CN_{Ca} , from 13.6 to 15.0, while CN_{Mg} and CN_{Cu} remain unchanged at ≈ 12.5 and ≈ 10.4 , respectively. The partial coordination numbers depend on alloy composition, so that the number of Ca atoms decreases, the number of Cu atoms increases and the number of Mg atoms is almost constant with increasing TM concentration. Voronoi tessellation shows that many types of coordination polyhedra are present, but the most common are Kasper and distorted Kasper polyhedra at the favorable CNs. The fractions and distributions of these clusters depend on alloy composition. Polytetrahedral- type clusters and five-coordinated vertices dominate in the amorphous structures; this indicates that tetrahedra and pentagonal bi-pyramids are the main building blocks in these amorphous alloys.

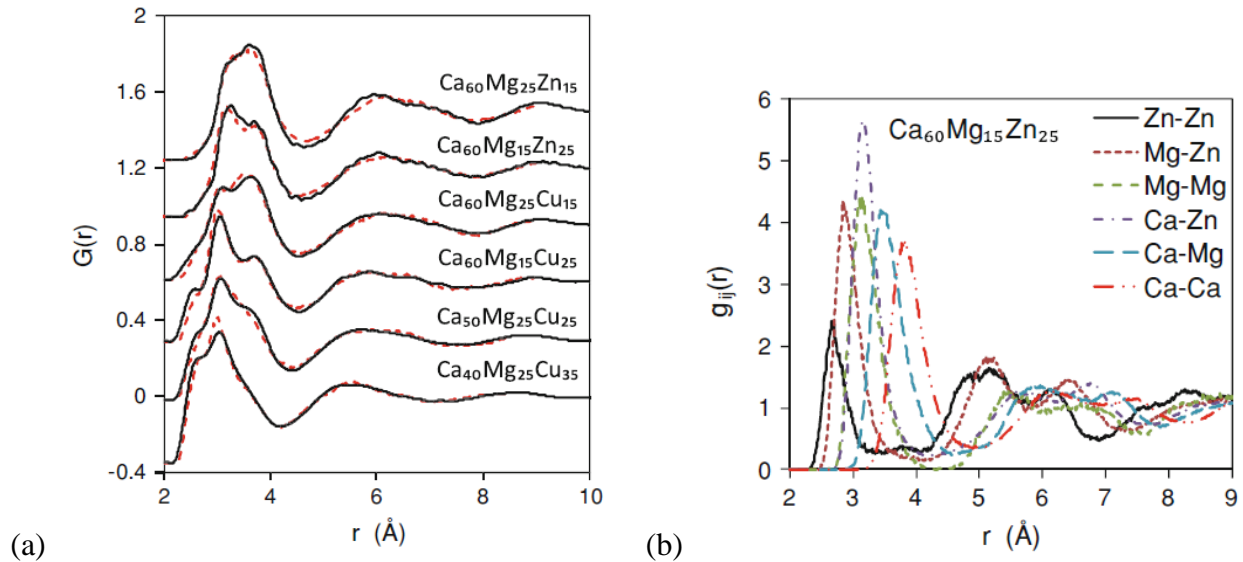


Figure 9: (a) Experimental (solid lines) and QMD-simulated (dashed lines) total radial distribution functions, $G(r)$, of Ca-Mg-Zn and Ca-Mg-Cu amorphous alloys. (b) QMD-simulated partial radial distribution functions, $g_{ij}(r)$, for $Ca_{60}Mg_{15}Zn_{25}$.

3.2.2.2 MD Simulation of the Structure and Transport Properties of Cu-Zr Metallic Liquids

There has been a large amount of discussion in the past decade as to whether the structure of metallic liquid contributes to its ability to form a glass upon cooling. This idea dates back to a hypothesis by Frank that the stability of supercooled liquids can be explained by the prevalence of efficiently packed clusters that have symmetry incompatible with crystal formation and that icosahedrally coordinated clusters fill this role for single element systems. More recent studies have considered how these efficiently packed clusters group together to form medium-range order in metallic glasses. Along with the energetic stability provided by these clusters, their

effect on atomic mobility in the supercooled liquid has also been studied as a contributing reason for glass formation in metals. In particular, there has been a focus on the role of icosahedrally coordinated clusters as a basis for beneficial structural order. These clusters were found to be present in supercooled liquids of multicomponent alloys using x-ray diffraction. Via atomistic simulation, it was found that these clusters tend to form large, interconnecting networks in compositions known for forming bulk metallic glasses. That discovery has spurred a focus towards determining whether icosahedral clusters lead to slowed diffusion and, therefore, bulk metallic glass formation. In particular, it has been shown that the slowest atoms in a Cu-Zr liquid are generally associated with icosahedral clusters. It is also known that these clusters tend to agglomerate and form medium-range order, which has been found to further reduce atomic mobility in the liquid. Consequently, it is theorized that the formation of icosahedral short-range order and networks can contribute to glass formation in at least Cu-Zr-based alloys.

In this work, we take a critical look at this structural component of glass-forming ability using the Cu-Zr binary as a trial system [13]. We use molecular dynamics to show how structure changes with composition and attempt to draw trends with glass-forming ability. Additionally, we study the evolution of the amorphous structure with temperature during a constant-pressure quench from the liquid. We also perform a rapid quench from the liquid followed by evolution at a constant volume and temperature to decouple the effects of temperature and density change from the effect of structural rearrangement. Our overall goal is to assess whether the present theories can be used to help explain glass-forming ability and structural rearrangements during cooling in this system. We then explore packing efficiency and “defective” clusters as a more generalized structural explanation. We found that the development of the icosahedral order fails to explain the observed diffusivity and energy changes in the Cu-Zr system. Instead we found that ideally packed atomic clusters are formed at the expense of clusters with excess or deficient free-volume during structural relaxation of a metallic glass (Figure 10), which supports earlier work by Egami et al. [14]. The identified structural model also explains slowed diffusivity in compositions and alloy systems that do not show a propensity for forming icosahedrally coordinated clusters and provides a framework for understanding why the formation of networks of icosahedral clusters is correlated with slowed dynamics.

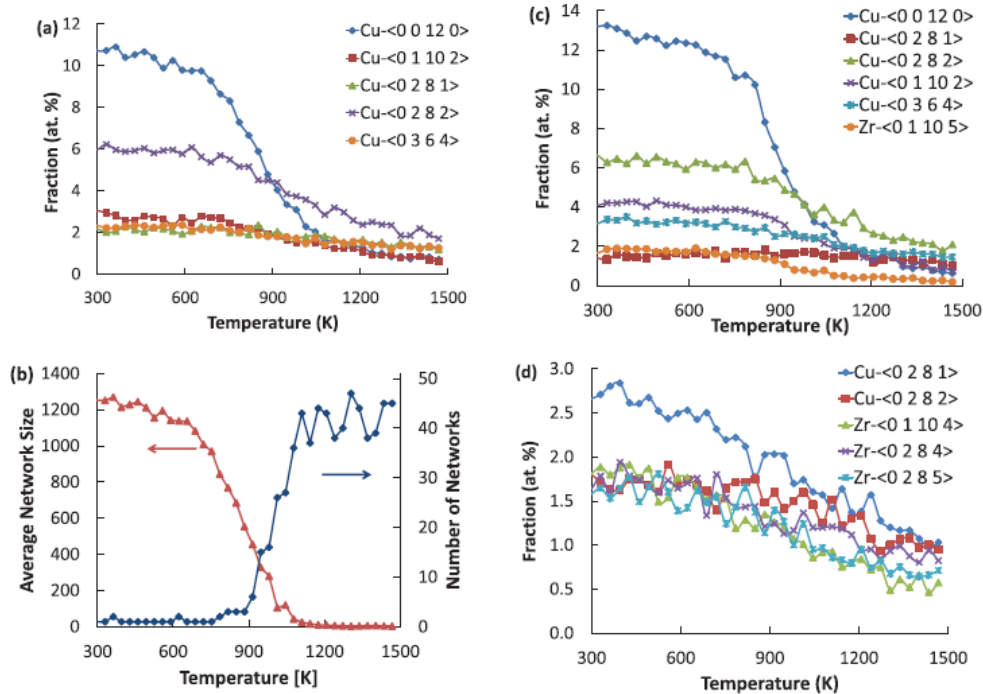


Figure 10: (a) The most prevalent clusters by Voronoi index and (b) average size and number of networks of icosahedral clusters in a $\text{Cu}_{64.3}\text{Zr}_{35.7}$ metallic glass as a function of temperature during a quench at 1011 K/s. The most prevalent clusters during cooling for (c) $\text{Cu}_{70}\text{Zr}_{30}$ and (d) $\text{Cu}_{30}\text{Zr}_{70}$ are also shown.

3.3 Alloy Processing and Characterization

3.3.1 Solid State Joining

3.3.1.1 Inertia Friction Welding of Dissimilar Superalloys Mar-M247 and LSHR

Many advanced applications require different sections of a single structural component to operate in very different temperature and loading conditions. An attractive way to fulfill this requirement is to design and fabricate a hybrid structure consisting of several superalloys joined together. In such design, sections operating under high loading conditions, but at lower temperatures, are made of a PM alloy, while sections requiring outstanding creep resistance at higher temperatures are made of a cast alloy. One method that can be utilized to produce complex geometries and hybrid structures from Ni superalloys is welding. Unfortunately, traditional fusion welding techniques generally cannot be used for Ni superalloys, which have high volume fractions of γ' particles, as these result in welding defects such as liquation cracking, strain age cracking, etc.

In this work, inertia friction welding (IFW) was used to weld two dissimilar Ni-based superalloys, LSHR, and Mar-M247. LSHR is a high-strength PM alloy for operation up to temperatures between $\sim 700\text{ }^\circ\text{C}$ and $740\text{ }^\circ\text{C}$ and Mar-M247 is a casting alloy developed for applications requiring high strength and creep resistance at elevated temperatures up to $1000\text{ }^\circ\text{C}$ [15]. The strength of both alloys is mainly controlled by γ' particles and also enhanced by solid solution and grain-boundary strengthening. Very different mechanical properties make IFW of

these superalloys challenging. Because IFW of these alloys was carried out for the first time, different IFW conditions were tried in effort to develop suitable welding parameters. Several IFW samples were produced and their microstructure and properties were examined. In this work, the welding behavior, as well as microstructure and microhardness, of the welded superalloys are reported. The following results were obtained.

The Mar-M247 alloy had higher tensile strength than the LSHR alloy at the applied IFW conditions. The true plastic forging strain rate and total forging strain of the LSHR alloy at the IFW interface occurred under the applied axial forging force were 1.94 and 0.39/s, respectively; this resulted in the formation of a characteristic flash. The true plastic forging strain and strain rates of the Mar-M247 alloy at the IFW interface were about 18 times lower, only 0.11 and 0.022/s, respectively.

Three stages of the IFW process occurring at different angular deceleration and friction conditions were identified. During the first stage, the coefficient of friction and the friction torque had almost constant and low values indicating friction sliding of mating surfaces. During this stage, the temperature at the contact surfaces rapidly increased, initiating local plastic deformation under the applied axial load. During the second stage, which started after the rotation speed decreased to some level, the friction coefficient and angular deceleration rapidly increased forcing the flywheel to stop rotating. At this stage, welding of two alloys occurred. The third stage occurred under the applied axial force at no rotation and was associated with further sample upset and diffusion bonding under cooling conditions.

During IFW, transition from the composition of the Mar-M247 alloy to the composition of the LSHR alloy occurred in a narrow, ~8 to 23 μm thick layer located mainly on the LSHR side of the weld interface. It is likely that both mechanical mixture due to severe plastic deformation at the mating surfaces and grain-boundary diffusion of the elements during the IFW process were responsible for the observed distribution of the alloying elements at the weld interface. A heat affected zone (HAZ) was recognized through a strong dependence of the microhardness and the volume fractions of the primary γ' particles on the distance from the weld interface. The HAZ thickness was ~4.5 to 6.0 mm and consisted of ~2.0 to 3.5 mm thick layers on both the Mar-M247 and LSHR alloy sides from the weld interface. In the HAZ, microhardness of the Mar-M247 alloy continuously increased with a decrease in the distance from the weld interface from $H_v = 405$ typical to the property of the virgin alloy to $H_v = 527$ at the interface. At the same time, microhardness of the LSHR alloy was 464 H_v outside the HAZ, showed a local minimum of 439 H_v at $L = 1.1$ mm from the interface and rapidly increased to $H_v = 568$ at the weld interface. The microhardness dependence on the distance from the weld interface was explained by the evolution of the γ' particles during and after IFW.

Noticeable dissolution of the primary γ' particles and grain refinement occurred in both alloys inside the HAZ. The size and volume fraction of the primary γ' rapidly decreased with a decrease in the distance from the interface from their original values of 64 pct (Mar-M247) and 35 pct (LSHR) outside HAZ to ~30 pct (Mar-M247) and 0 pct (LSHR) at the weld interface. A 60 to 100 μm thick precipitate-free region was detected on the LSHR side of the weld interface. The grain size in the LSHR alloy was ~3.5 μm outside the HAZ, decreased to ~1.4 μm at $L = 0.33$ mm and slightly increased to 1.9 μm at the weld interface. Large elongated grains of the cast Mar-M247 alloy transformed into finer and more equiaxed grains inside the HAZ. A 5 to 30

μm thick layer of very fine ($\sim 0.5 \mu\text{m}$ in diameter) grains was formed on the Mar-M247 side of the weld interface. Nanometer-sized oxide and carbide particles, agglomerated/clustered into semi-continuous thin films, were observed at the flat regions of the weld interface in the middle and rim sections of the weld sample (Figure 11). These nano-particles seemed to form during the first IFW stage due to the surface oxidation and grinding/milling by friction. Their clustering was likely to occur due to insufficient plastic flow of the Mar-M247 alloy in the radial direction, which did not allow these particles to move into the flash.

A radial crack contaminated with nanometer oxide and carbide particles was observed in the rim section of the welded sample on the Mar-M247 side adjacent to the well-welded interface (Figure 11). The analysis of the weld conditions and microstructure suggested that the crack formed during the second stage of the angular deceleration, when the alloys were already welded, but the flywheel still had remaining kinetic energy to plastically shear the weld interface region and for the crack to initiate and propagate inside the lower ductility Mar-M247 alloy. It was suggested that the rotation should be stopped as soon as the friction torque reaches a critical value to prevent the torsional-deformation-induced after welding fracture.

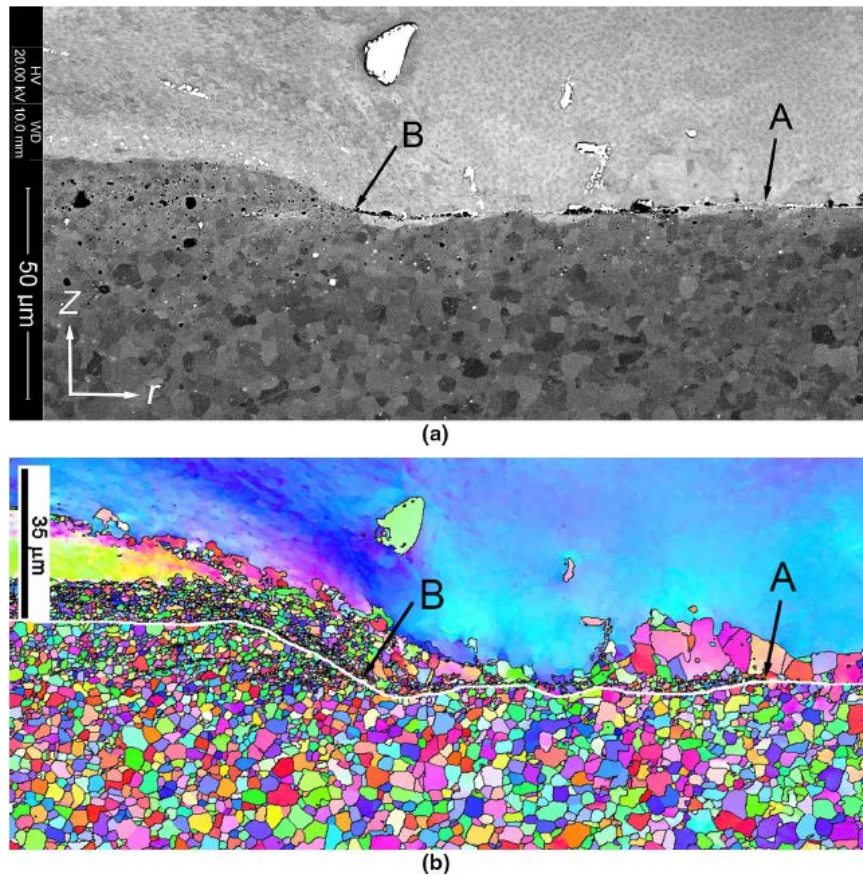


Figure 11: (a) Backscatter electron image and (b) inverse pole figure map of the IFW region showing transition from a flat (right) to wavy (left) weld interface appearance. The weld interface is outlined by a white line in figure (b). The LSHR alloy is below the IFW interface and it is darker than the Mar-M247 alloy in figure (a).

3.3.2 Characterization of γ' Precipitates in Ni-based Superalloys

A methodology for determining the preferred site occupancy of various alloying elements within ordered γ' precipitates was developed and applied to Rene88 samples [16]. The method utilized atom probe tomography (APT) and x-ray diffraction techniques with controlled monochromated synchrotron beams to determine element positions. Samples were solutionized at 1150 °C for 30 minutes and cooled at 24 °C/min with subsequent aging at 760 °C. The APT techniques provided composition data critical for modeling the potential lattice locations within the γ' . Analysis of the synchrotron data obtained at the energies corresponding to the absorption edges of Cr, Co, and Nb (Figure 12) identified the preference for Nb to reside at the Al sublattice sites, Cr to reside in the Ni sublattice sites, and Co to share both sides within the ordered γ' phase. Careful alignment of the APT samples provided identification of the (100) planes and allowed comparison of Ti, Ni, Al, and Cr site preferences by overlaying composition vs position data. Both Ti and Cr preferentially resided at Al sublattice sites within the ordered γ' . Cobalt did not appear to show a strong specific site preference. However, the small amount of Co present in the γ' phase, coupled with detection efficiency in the atom probe, severely restricts the analysis of this alloying element within the γ' phase. Additional data, employing synchrotron energies that will suppress the remaining elements (Ti, Mo, and W), are required to complete the comparisons of the diffraction intensities. APT characterization with samples oriented to align specific planes within γ' relative to the detector is also required to provide experimental validation and secondary γ' composition.

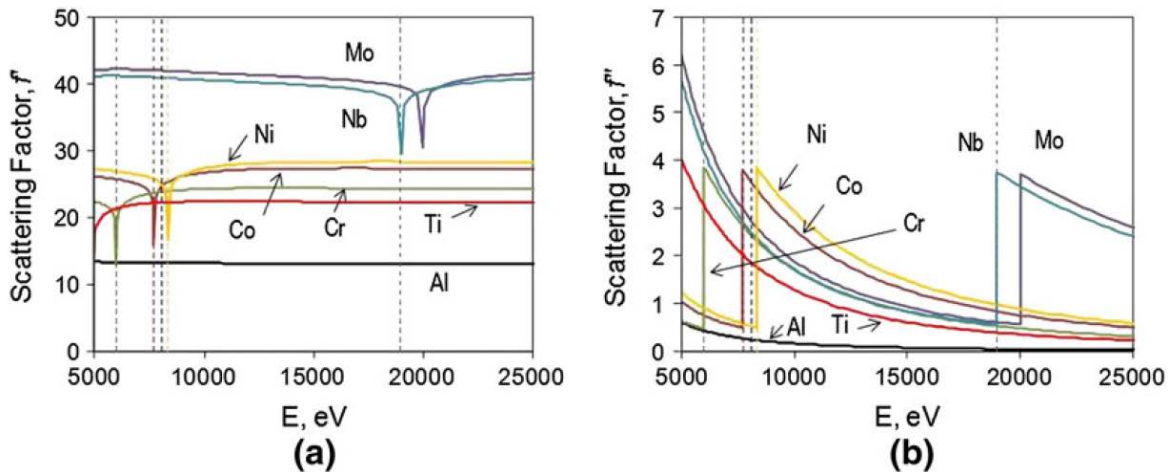


Figure 12: (a) True (f') and (b) imaginary (f'') parts of the X-ray scattering factors for Al, Co, Cr, Mo, Nb, Ni, and Ti in the X-ray energy range of 5000–25000 eV. The vertical lines correspond to the energies used in this work.

3.4 Alloy Processing and Characterization

3.4.1 Thermal Transport in Copper/Diamond System

For reliable operation of high power density electronic devices, an efficient heat removal from hot regions is required. The high thermal conductivity (λ) and low coefficient of thermal expansion (CTE) of Cu-diamond composites make them preferred materials for these heat sink

applications. Consequently, this composite system has been the subject of extensive investigation in recent years. Maximization of the metal/diamond interface thermal conductance (h_c) is a promising path to improve the composite λ . Therefore, examinations of h_c for Cu/diamond interface and factors influencing it are both of scientific interest and practical importance.

In the absence of an interface layer between Cu and diamond, h_c for Cu/diamond interfaces are quite low and this causes λ of composites also to be very low. For example, one prior study reported $\lambda = 215$ W/m-K for a Cu-42 vol% diamond composite with no interfacial layer. In this case, λ for the composite is significantly lower than for Cu (~ 400 W/m-K). Thus, in this example, the addition of diamond in Cu matrix leads to a deterioration of the ability to spread heat rather than the desired improvement. For this particular composite, h_c was calculated to be 0.5 MW/m²-K and this low value of h_c resulted in the low λ . The introduction of a thin interfacial carbide (*e.g.* Cr₃C₂, B₄C, TiC, etc.) layer between Cu and diamond has been shown to increase the λ of Cu-diamond composites to values well above that of Cu, which is effected due to the improvement in h_c . It has also been established that h_c is inversely related to the thickness of interfacial carbide layer. The calculation of h_c in prior studies invoked Hasselman-Johnson and/or differential effective medium (DEM) models, which require the composite λ to be one of the input parameters.

There is an alternate method, time-domain thermoreflectance (TDTR), to determine h_c for metal/diamond interfaces, which allows precise and more direct measurement for an individual interface rather than an average over a bulk sample. The sample for TDTR examination can be prepared by deposition of thin metallic layers (~ 90 nm thick) on a diamond substrate. The metal layers are locally heated (temperature increase is ≤ 1 K) with a pump laser beam, and the change in its reflectance with time and temperature is monitored with a probe laser beam. The modeling of changes in reflectance of metal top layers leads to the determination of h_c . Several studies have employed TDTR or similar techniques to determine h_c for metal/diamond interfaces. Recent advances with two-color TDTR have greatly improved the characterization of specimens with a Cu top layer. One prior study reported an $h_c \sim 60$ MW/m²-K for an interface between Cu and highly oriented pyrolytic graphite (HOPG), whereas another prior study reported an $h_c \sim 35$ MW/m²-K for an interface between Cu and diamond. There are no prior reports on TDTR-determined h_c for a material system, where an interface layer is introduced between Cu and diamond.

In the current research, a Ti interface layer is introduced between Cu and diamond, and the h_c for this material system is determined with TDTR. The objective of this study is to determine if the presence of a Ti interface layer improves the h_c , akin to an enhancement effected by carbide interface layers in the case of Cu-diamond composites [17]. Furthermore, the thickness of Ti interface layer is systematically varied and the h_c is determined using TDTR for different Ti layer thicknesses. This part of study was aimed at identifying any correlations between h_c and the Ti interface layer thickness. A prior study has used molecular-dynamics simulations to demonstrate that the strength of the potential binding metal to the substrate has a significant effect on the predicted h_c , with a higher strength resulting in a higher h_c . Transition metals such as Ti and Cr bond strongly to carbon and moreover, Ti has a stronger bond with carbon than Cr. Furthermore, it has been shown experimentally that other carbon-based material has a slightly higher h_c with Ti than with Cr, despite a better matching of vibrational density of states with Cr

than with Ti. Therefore, Ti was selected as the interface layer between Cu and diamond in the current study.

In a seminal paper on this topic, it was concluded that bulk disorder near the interface can cause significant deviations in the experimentally determined h_c from its model prediction. In the current study, the concentrations of nitrogen and other impurities (*e.g.* hydrogen, oxygen, etc.) were measured as these may contribute to the disorder. Secondary ion mass spectrometry (SIMS) was used for concentration measurements as a function of depth below the sample surface (Figure 13). Atomic force microscopy (AFM) was used to measure the surface roughness of diamond substrates. The differences in h_c of specimens with synthetic and natural diamond substrates are discussed in the context of variations in near-surface disorder and interface roughness.

The interface thermal conductance between Cu and diamond was measured using TDTR method. Very thin Ti interface layers (≤ 3.5 nm thick) were introduced between Cu and diamond, and the effects on h_c of presence of Ti at the interface as well as variation in its thickness were examined. The specimens for TDTR characterization were prepared via magnetron sputtering of metal layers (Cu and Ti) on synthetic and natural single crystal diamond substrates. The results indicate that the values of h_c for specimens with synthetic diamond substrate are $\sim 2\times$ higher than for specimens with natural diamond substrate (Figure 14). This difference can be attributed to a lower level of disorder in near-surface region of synthetic diamond substrate, as a result of significantly lower nitrogen concentration than natural diamond. Furthermore, the presence of a Ti-interface layer increases the h_c in specimens with either synthetic or natural diamond substrate. The h_c is directly related to the Ti-interface layer thickness, within the range of thicknesses examined in the current study. An enhanced adhesion of Cu top layer with increasing Ti-interface layer thickness causes an increase in h_c .

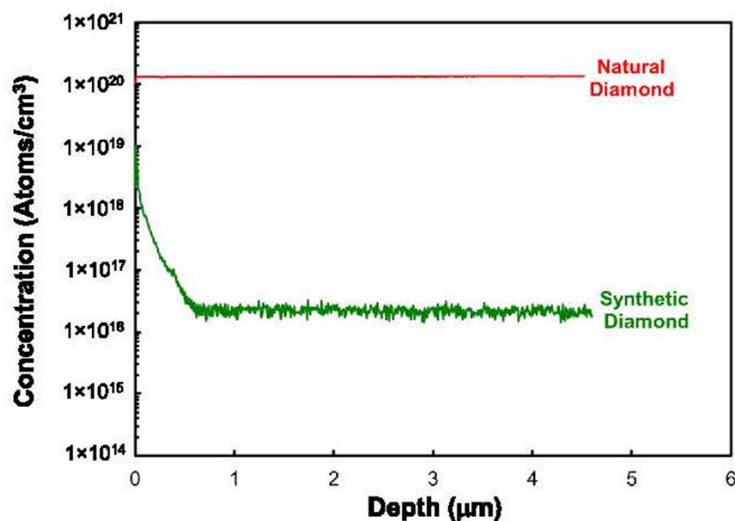


Figure 13: SIMS depth profiles showing nitrogen concentration as a function of depth below the surface for synthetic and natural diamond substrates.

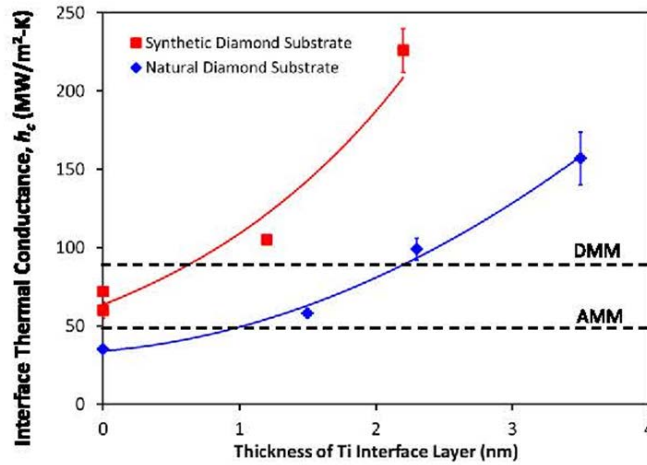


Figure 14: Effect of Ti Interface Layer Thickness on Cu/Diamond Interface Thermal Conductance. The solid lines depict the approximate trend for experimental data points. The dotted horizontal lines depict the predictions of acoustic mismatch and diffuse mismatch models (AMM and DMM) for Cu/diamond interface.

References

- [1] S.I. Rao, D.M. Dimiduk, J.A. El-Awady, T.A. Parthasarathy, M.D. Uchic, and C. Woodward, "Screw dislocation cross-slip at cross-slip plane jogs and screw dipole annihilation in FCC Cu, Ni investigated via atomistic simulations," *Acta Materialia*, v 101, pp 10-15, 2015.
- [2] B. Wilshire and P.J. Scharning, "Theoretical and practical approaches to creep of Waspaloy," *Materials Science & Technology*, v 25, 2015, pp 242-248.
- [3] T.P.Gabb, J Gayda, J. Telesman, and P.T.Kantzos, "Thermal and Mechanical Property Characterization of the Advanced Disk Alloy LSHR," NASA Tech Report, NASA/TM-2005-213645, 2005.
- [4] O.N. Senkov, S.V. Senkova, C. Woodward, and D.B. Miracle, "Low-density, refractory multi-principal element alloys of the Cr-Nb-Ti-V-Zr system: Microstructure and phase analysis," *Acta Materialia*, v 61, 2013, pp 1545-57.
- [5] O.N. Senkov, S.V. Senkova, D.B. Miracle, and C. Woodward, "Mechanical properties of low-density, refractory multi-principal element alloys of the Cr-Nb-Ti-V-Zr system," *Materials Science and Engineering A*, v 565, 2013, pp 51-62.
- [6] O.N. Senkov, F. Zhang, and J.D. Miller, "Phase Composition of a CrMo_{0.5}NbTa_{0.5}TiZr High Entropy Alloy: Comparison of Experimental and Simulated Data," *Entropy*, v 15, 2013, pp 3796-809.
- [7] O.N. Senkov, C. Woodward, and D.B. Miracle, "Microstructure and Properties of Aluminum-Containing Refractory High-Entropy Alloys," *JOM*, v 66, 2014, pp 2030-42.
- [8] O.N. Senkov, S.V. Senkova, and C. Woodward, "Effect of aluminum on the microstructure and properties of two refractory high-entropy alloys," *Acta Materialia*, v 68, 2014, pp 214-28.
- [9] D.B. Miracle, J.D. Miller, O.N. Senkov, C. Woodward, M.D. Uchic, and J. Tiley, "Exploration and Development of High Entropy Alloys for Structural Applications," *Entropy*, v 16, 2014, pp 494-525.
- [10] O.N. Senkov, J.D. Miller, D.B. Miracle, and C. Woodward, "Accelerated exploration of multi-principal element alloys with solid solution phases," *Nature Communications*, v 6, 2015, pp 6529.
- [11] O.N. Senkov, J.D. Miller, D.B. Miracle, and C. Woodward, "Accelerated exploration of multi-principal element alloys for structural applications," *Calphad: Computer Coupling of Phase Diagrams and Thermochemistry*, v 50, 2015, pp 32-48.
- [12] O.N. Senkov and Y.Q. Cheng, "Ab Initio Molecular Dynamics Simulation of the Amorphous Structure of Ca-Mg-Cu and Ca-Mg-Zn Alloys," *Metallurgical and Materials Transactions A*, v 44, 2013, pp 1980-1989.

[13] L. Ward, D. Miracle, W. Windl, O.N. Senkov, and K. Flores, "Structural evolution and kinetics in Cu-Zr metallic liquids from molecular dynamics simulations," *Physical Review B*, v 88, 2013, pp. 134205/1-10.

[14] T. Egami, V.A. Levashov, J.R. Morris, and O. Haruyama, "Statistical Mechanics of Metallic Glasses and Liquids," *Metallurgical and Materials Transactions A*, vol. 41, 2010, pp 1628-1633.

[15] O.N. Senkov, D.W. Mahaffey, S.L. Semiatin, and C. Woodward, "Inertia Friction Welding of Dissimilar Superalloys Mar-M247 and LSHR," *Metallurgical and Materials Transactions A*, v 45, 2014, pp 5545-61.

[16] J.S. Tiley, O. Senkov, G. Viswanathan, S. Nag, J. Hwang, and R. Banerjee, "A methodology for determination of g' site occupancies in nickel superalloys using atom probe tomography and X-ray diffraction," *Metallurgical and Materials Transactions A*, v 44, 2013, pp 31-38.

[17] V. Sinha, J.J. Gengler, C. Muratore and J.E. Spowart, "Effects of Disorder State and Interfacial Layer on Thermal Transport in Copper/Diamond System," *Journal of Applied Physics*, v 117, no 7, 2015, pp 074305.

List of Acronyms

Acronym/ Abbreviation	Description
ADVENT	Adaptive Versatile Engine Technology
AFM	Atomic Force Microscopy
AFRL	Air Force Research Laboratory
AMM	Acoustic Mismatch Model
APB	Anti-Phase Boundary
APT	Atom Probe Tomography
BCC	Body-Centered Cubic
BMG	Bulk-Metallic Glass
CALPHAD	Calculation of Phase Diagrams
CN	Coordination Number
CSRC	Coefficient of Thermal Expansion Clustering
CSRO	Chemical Short Range Ordering
CTE	Coefficient of Thermal Expansion
DD	Discrete Dislocation
DEM	Differential Effective Medium
DMM	Diffuse Mismatch Model
DSC	Differential Scanning Calorimetry
EBS	Electron Back Scattered Diffraction
FCC	Face-Centered Cubic
FEA	Finite-Element Analysis
FEM	Finite-Element Method
FIB	Focused Ion Beam
GBS	Grain Boundary Sliding

Acronym/ Abbreviation	Description
GFA	Glass-Forming Ability
GL	Glide Locks
HAZ	Heat Affected Zone
HC	Thermal Conductance
HEA	High-Entropy Alloys
HEETE	Highly Efficient Embedded Turbine Engine
HIP	Hot Isostatic Pressing
HL	Hirth Locks
ICMSE	Integrated Computational Materials Science and Engineering
IFW	Inertia Friction Welding
IHPRPT	Integrated High Performance Rocket Propulsion Technology
IM	Intermetallic
INVENT	Integrated Vehicle Energy Technology
LC	Lomer-Cottrell
LSHR	Low Solvus High Refractory
MD	Molecular Dynamics
MGs	Metallic Glasses
MMF	Maxwell Mean-Field
MPEA	Multi-principle element alloys
NEB	Nudged Elastic Band
OIM	Orientation Imaging Microscopy
P1	Principal Stress
PRDF	Partial Radical Distribution Function
QMD	Quantum Molecular Dynamics

Acronym/ Abbreviation	Description
R&D	Research and Development
RDF	Radical Distribution Function
RMC	Reverse Monte Carlo
SEM	Scanning Electron Microscope
SIMS	Secondary Ion Mass Spectrometry
SRO	Short Range Order
TDTR	Time-Domain ThermoReflectance
UTS	Ultimate Tensile Strength
VAATE	Versatile Affordable Advanced Turbine Engine
YS	Yield Strength